Title	Design principles of permanent magnet dual-memory machines
Author(s)	LI, F; Chau, KT; Liu, C; ZHANG, Z
Citation	IEEE Transactions on Magnetics, 2012, v. 48 n. 11, p. 3234-3237
Issued Date	2012
URL	http://hdl.handle.net/10722/189033
Rights	©2012 IEEE. Personal use of this material is permitted. However, permission to reprint/republish this material for advertising or promotional purposes or for creating new collective works for resale or redistribution to servers or lists, or to reuse any copyrighted component of this work in other works must be obtained from the IEEE.

Design Principles of Permanent Magnet Dual-Memory Machines

Fuhua Li, K. T. Chau, Chunhua Liu, and Zhen Zhang

Department of Electrical and Electronic Engineering, The University of Hong Kong, Hong Kong, China

The permanent magnet (PM) dual-memory machine incorporates the concept of PM memory machines and PM hybrid machines, hence offering the flexible flux-tuning and flux-mnemonic function. It employs the aluminum-nickel-cobalt (Al–Ni–Co) and neodymium-iron-boron (Nd–Fe–B) PMs as a PM group embedded in each PM pole to complement each other. Thus, it inherently achieves the merit of high working temperature and high power density. Design principles of this new class of machines are devised and discussed. Both simulation and experimentation are given to demonstrate the validity of the proposed design principles.

Index Terms—**Dual-memory machine, memory machine, flux-mnemonic machine, permanent magnet machine.**

I. Introduction

THE permanent magnet (PM) dual-memory machine is derived from the incorporation of three kinds of machines, including the AC-excited PM memory machine [1], [2], the dc-excited PM memory machine [3], [4] and the PM hybrid machine [5], [6]. The key feature of this dual-memory machine is that it utilizes one PM group involving two different kinds of PM materials embedded in each PM pole, instead of using one kind of PM material in the aforementioned PM memory machines.

The PM materials used in this machine are the aluminum-nickel-cobalt (Al–Ni–Co) and the neodymium-iron-boron (Nd–Fe–B). The Al–Ni–Co PM is used to perform the online flux-tuning function, namely online magnetization and demagnetization, due to its low coercivity. The Nd–Fe–B PM is used to provide an auxiliary magnetic field complementing the Al–Ni–PM to achieve the aim of high power density and high efficiency with the flexible flux control ability. Furthermore, the Al–Ni–Co PM has the merit of high working temperature limit of 450–550 °C, in contrast with 80–180 °C of the Nd–Fe–B PM. Thus, the Al–Ni–Co PM shows the merit of keeping the machine at good performance even when the working condition has a large fluctuation in temperature in a short period. On the other hand, the Nd–Fe–B PM has the superiority of large magnetic energy product with a linear demagnetization curve which enables the machine to work with heavy load. The combination of these two kinds of PM material enables the machine to incorporate their individual merits and thus improves the overall performance.

The purpose of this paper is to devise the design principles of this class of PM dual-memory machines. Design equations will be derived and hence the design process will be discussed. Both simulation and experimentation results will be given to verify the proposed design principles.

II. Design Principles

Fig. 1 shows the basic structure of the PM dual-memory machine. Since this machine is a new class of PM machines, a set of systematic design principles is highly essential. Particularly, it needs to realize the principles on how to select the numbers of salient poles in the stator and rotor, how to calculate the sizes of PMs on each PM pole, and how to determine the rotor dimensions.

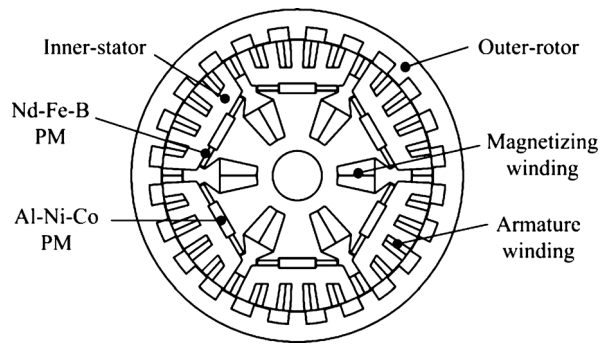

Fig. 1. PM dual-memory machine structure.

1) Salient Pole Numbers: The PM dual-memory machine employs the outer-rotor inner-stator structure with salient poles on both the rotor and stator. Similar to the switched reluctance machine, the salient pole numbers of the stator and rotor of this machine is governed by [4]

$$\begin{cases} N_s = 2mk \\ N_{\rm PM} = \frac{N_s}{m} \\ N_r = N_s \pm 2k \end{cases} \tag{1}$$

where N_s is the number of salient poles in the stator, N_r is the number of salient poles in the rotor, m is the number of phases, $N_{\rm PM}$ is the number of PM poles, and k is a positive integer. Larger values of N_s and N_r can smooth the output torque but increase the operation frequency. Similarly, the larger the number of phases, the smoother the output torque is resulted; but more space is occupied by armature windings, leading to increase the machine size.

2) PM Surface Areas: Fig. 2 shows the PM pole configuration. It can be seen that one PM group including three PM pieces is embedded in one PM pole. The overall PM surface area orthogonal to the magnetization direction is the sum of the surface areas of three PM pieces, which directly dictates the air-gap flux density.

Since each PM pole needs to perform online magnetization or demagnetization by the corresponding magnetizing winding, the stator is physically separated into $N_{\rm PM}$ pieces. For m-phase structure, the number of stator salient poles over each PM pole is

Manuscript received March 02, 2012; revised April 23, 2012; accepted May 07, 2012. Date of current version October 19, 2012. Corresponding author: K. T. Chau (e-mail: ktchau@eee.hku.hk).

Color versions of one or more of the figures in this paper are available online at http://ieeexplore.ieee.org.

Digital Object Identifier 10.1109/TMAG.2012.2199477

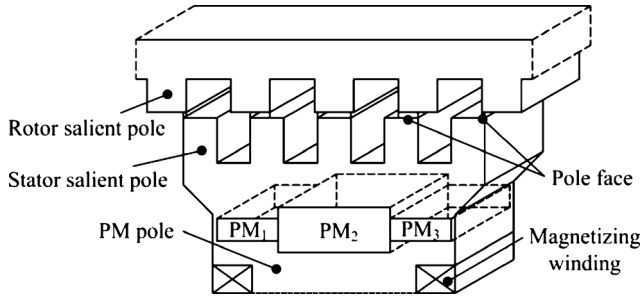

Fig. 2. PM pole configuration.

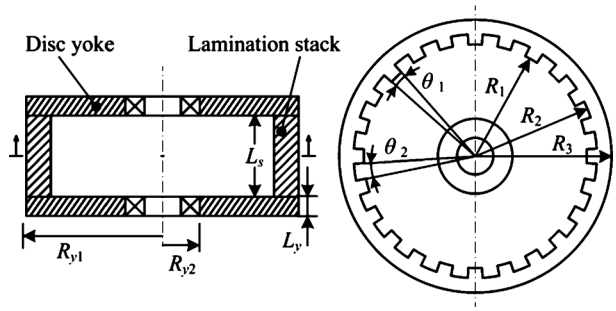

Fig. 3. Outer-rotor structure.

equal to m. In this design, m is selected as five so as to provide a smooth output torque and also the possibility of fault-tolerance operation, leading to the use of 5 stator salient poles over one PM pole.

The total pole face area of the stator per PM pole S_{fa} is a key design parameter which governs the air-gap flux density and hence the output torque. It can be expressed as follows:

$$S_{fa} = \sum_{i=1}^{m} S_i = k_A(S_{\mathrm{PM1}} + S_{\mathrm{PM2}} + S_{\mathrm{PM3}}), \quad (k_A < 1) \tag{2}$$

where S_i is the pole face area of individual stator salient pole within one PM pole, m is the number of phases or salient poles over one PM pole, k_A is the area coefficient, and $S_{\mathrm{PM1}}, S_{\mathrm{PM2}}$ and S_{PM3} are the surface areas of three PM pieces, respectively. Since the magnetic flux always tends to pass the shortest way with the smallest reluctance, this surface area is equivalent to the air-gap area through which the flux goes from the PM group to the rotor. Thus, S_{fa} can be used to determine the necessary surface area of PM pieces. Taking into account the magnetic fringing effect, k_A should be less than unity to ensure the air-gap flux density not less than the PM remanence.

On the other hand, when the Al–Ni–Co PM piece is placed in between two Nd–Fe–B PM pieces to provide the magnetic field in parallel, S_{PM1} equals S_{PM3} while S_{PM2} is governed by the range of controllable air-gap flux density and also the size of magnetizing winding. Since the magnetization or demagnetization process can be finished within a short duration, the allowable current density of the magnetizing winding can be much higher than the standard 5 A/mm^2. Consequently, the required space to allocate the magnetizing winding can be minimized.

3) PM Thicknesses: The PM thickness directly dictates the MMF provided by the PM. So, the three PM thicknesses of each PM group are an important issue of this dual-memory machine. Since the two thicknesses of the Nd–Fe–B PM pieces are the same, the thickness of the Al–Ni–Co PM piece and the thickness proportion between the Al–Ni–Co and Nd–Fe–B PM pieces are determined in such a way that the Al–Ni–Co PM piece can be online magnetized to different magnetization levels while the Al–Ni–Co PM thickness can withstand the demagnetization field of the neighboring Nd–Fe–B PM pieces.

By applying the Thevenin's theorem to the magnetic circuit of this machine, the Al–Ni–Co PM MMF under forward magnetization and backward magnetization can be expressed as follows:

$$F_{fm} = K_m F_{\mathrm{mag}} - K_{\,n} F_{Nd} \tag{3}$$

$$F_{bm} = K_m F_{\mathrm{mag}} + K_{\,n} F_{Nd} \tag{4}$$

$$\frac{K_m}{K_n} = \frac{R_{Nd}}{R_\delta} \tag{5}$$

where F_{fm} and F_{bm} are the Al–Ni–Co PM MMF under forward magnetization and backward magnetization, respectively, K_m and K_n are the coefficients related to the Nd–Fe–B PM reluctance and air-gap reluctance, respectively, F_{mag} is the magnetizing winding MMF, F_{Nd} is the Nd–Fe–B PM MMF, R_{Nd} is the Nd–Fe–B PM reluctance, and R_δ is the air-gap reluctance. It can be observed from (3) and (4) that the forward magnetization requires a larger magnetizing MMF than the backward magnetization, which is due to the fact that the Nd–Fe–B PM pieces tend to help demagnetize or reversely magnetize the Al–Ni–Co PM piece.

4) Rotor Dimensions: In this machine, the outer-rotor is only made of iron, without any PMs or windings. Fig. 3 shows the outer-rotor structure, including the lamination stack and laminated sheet. Being the only rotating part of the machine, the rotor dissipates the electromagnetic torque during acceleration as governed by

$$J_{rs} = \frac{1}{4}\rho L_s N_r \left[\theta_1 \left(R_3^4 - R_1^4\right) + \theta_2 \left(R_3^4 - R_2^4\right)\right] \tag{6}$$

$$J_{ry} = \pi \rho L_y \left(R_{y1}^4 - R_{y2}^4\right) \tag{7}$$

$$T_r = (J_{rs} + J_{ry})\beta_r \tag{8}$$

where J_{rs} and J_{ry} are the moments of inertia of the lamination stake and disc yoke, respectively, L_s and L_y are the axial length of the stake and yoke, respectively, ρ is the mass density of iron, θ_1 and θ_2 are the pole arc and slot arc of the rotor, respectively, R_1, R_2 and R_3 are the inside radius, slot radius and outside radius of the rotor, respectively, R_{y1} and R_{y2} are the outside radius and inside radius of the disc yoke, T_r is the consumed torque by the rotor, and β_r is the angular acceleration of the rotor. It is obvious that the larger the value of the moment of inertia, the slower the acceleration is resulted. Meanwhile, a larger moment of inertia reduces the cogging torque and smoothes the output speed variation as given by

$$\Delta t = \frac{J_{rs} + J_{ry}}{T_r} \Delta\omega \tag{9}$$

where Δt is the time variation and $\Delta\omega$ is the angular speed variation.

Once the inner-stator diameter and air-gap length are fixed, the inside diameter of the outer-rotor can readily be determined. Then, the rotor thickness T_{rth} is selected in such a way that it

TABLE I
KEY DESIGN DATA

Rated power (kW)	1.2
Rated voltage (V)	200
Air-gap length (mm)	0.6
Rotor salient pole number	24
Stator salient pole number	30
PM pole number	6
Stator pole arc (°)	6
Stator slot arc (°)	6
Rotor pole arc (°)	7
Rotor slot arc (°)	8
Rotor stack length (mm)	80
Rotor back iron thickness (mm)	14.4
Al-Ni-Co PM size (mm^3)	30×8×80
Nd-Fe-B PM size (mm^3)	17.4×4×80

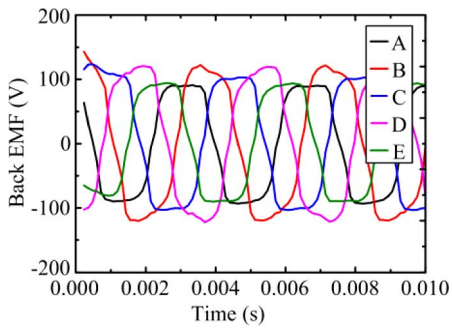

Fig. 4. Simulated back EMF waveforms at 700 rpm.

can accommodate the flux passing from the stator salient poles through the rotor salient poles as indicated by

$$T_{\mathrm{rth}} > \frac{S_{fa}}{2L_s} \tag{10}$$

where the factor 2 denotes that the flux is divided into two paths in the rotor. Another consideration of T_rth is to ensure the rotor having sufficient mechanical strength.

III. SIMULATION RESULTS

Based on the aforementioned design principles, a five-phase 1.2-kW outer-rotor PM dual-memory machine is designed in which the five phases, 30 stator salient poles, 24 rotor salient poles and 6 PM poles are governed by (1), while the stator dimensions, rotor dimensions and PM sizes are governed by (2)–(10). The key design data are listed in Table I.

In order to illustrate the validity of the proposed design principles, the designed machine is analyzed by using the time-stepping finite-element method (TS-FEM) in which the Al–Ni–Co PM is modeled by Preisach theory [7].

When the magnetizing winding of the machine is excited by 10 A to forward magnetize the Al–Ni–Co PM, the back electromotive force (EMF) waveforms operating at 700 rpm are simulated as shown in Fig. 4. It illustrates that the back EMF waveform is essentially trapezoidal so that the brushless dc operation is preferred, which is similar to other PM brushless dc machines. The corresponding magnitude and frequency agree with the aforementioned design principles of PM sizing and pole numbers. Additionally, it can be observed that the phases B and D have slightly higher amplitude than other three phases, which is actually due to the shape asymmetry among stator salient poles.

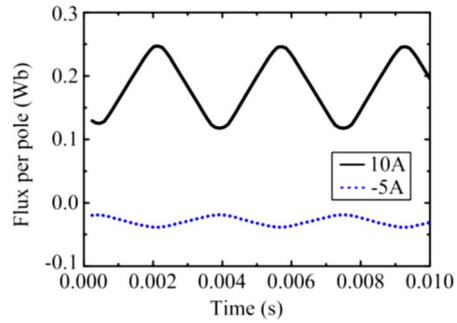

Fig. 5. Simulated flux per pole waveforms at 700 rpm under forward and backward magnetizations.

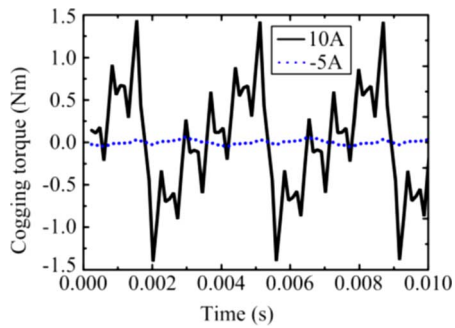

Fig. 6. Simulated cogging torque waveforms at 700 rpm under forward and backward magnetizations.

In order to illustrate the flux controllability of this machine, the magnetizing winding is first excited by a positive current of 10 A for forward magnetization of the Al–Ni–Co PM and then excited by a negative current of -5 A for backward magnetization of the Al–Ni–Co PM, the corresponding flux per pole waveforms operating at 700 rpm are simulated as shown in Fig. 5. It can be seen the overall flux is reversed, in the presence of controllable Al–Ni–Co PM and uncontrollable Nd–Fe–B PM, when the magnetizing current is reversed. It also indicates that the range of flux variation can be changed from 0.128 to 0.019 Wb, which verifies the effectiveness of the flux control based on the design principle described by (2)–(5).

In order to assess the effect of controllable flux on the cogging torque, the simulated cogging torque waveforms at 700 rpm under forward magnetization and backward magnetization are shown in Fig. 6. As expected, the cogging torque under forward magnetization is larger than that under backward magnetization because of the larger flux per pole. Even so, the corresponding peak value of cogging torque is about 1.4 Nm which is well accepted as compared with other PM brushless dc machines. It can be observed that there are five steps per cycle of the cogging torque waveform, which correspond to the existence of five phases. Also, the corresponding frequency agrees with the design of 6 PM poles, 30 stator salient poles, and 24 rotor salient poles.

When the machine drives the load torque of 5 Nm at 300 rpm, the simulated output torque waveform is shown in Fig. 7. It can be observed that the machine can provide the desired load torque of 5 Nm. The corresponding torque ripples are due to the

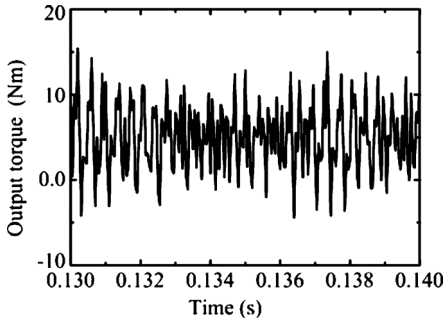

Fig. 7. Output torque waveform output at 300 rpm.

Fig. 8. Machine prototype.

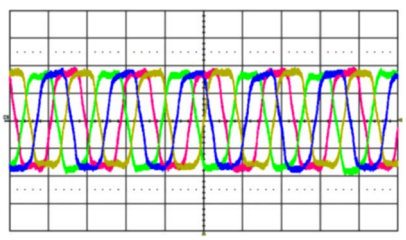

Fig. 9. Measured back EMF waveforms at 700 rpm (50 V/div, 2 ms/div).

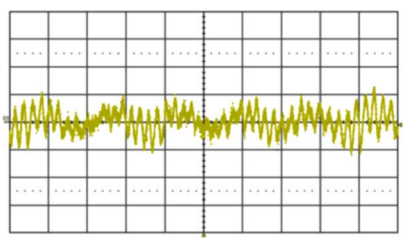

Fig. 10. Measured no-load torque waveform at 700 rpm (0.2 Nm/div, 50 ms/div).

cogging torques and commutation spikes that generally occur at PM brushless dc machines.

IV. Experimental Verification

The designed machine is prototyped and tested as depicted in Fig. 8. First, when the machine is driven to 700 rpm by the dynamometer, the back EMF waveforms are measured as shown in Fig. 9. They closely agree with the simulated waveforms in Fig. 4. Second, when the machine operates as a motor and runs at 700 rpm, the no-load torque waveform is measured by a dynamic torque transducer as shown in Fig. 10. It can be observed that the peak value is about 0.2 Nm, which is smaller than the simulated peak value of 1.4 Nm in Fig. 6. It is due to the fact that the dynamometer, torque transducer and couplings increase the effective moment of inertia which smoothes out the cogging effect. Third, when the machine drives a load torque of 5 Nm

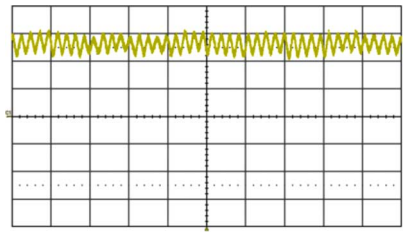

Fig. 11. Measured output torque waveform at 300 rpm (2 Nm/div, 50 ms/div).

and runs at 300 rpm, the output torque waveform is measured as shown in Fig. 11. It can be seen that the machine can provide the desired load torque of 5 Nm. As expected, the measured waveform has smaller torque ripples than the simulated ones in Fig. 7, which is again due to the smoothing effect of the additional moment of inertia of the dynamometer, torque transducer, and couplings.

Therefore, the experimental results well agree with the simulated results, hence verifying the validity of the proposed design principles of the PM dual-memory machine.

V. Conclusion

This paper has proposed and implemented the design principles for a new class of PM dual-memory machines. The key principles include how to select the numbers of salient poles in the stator and rotor, how to size the surface areas and thicknesses of three PM pieces (one Al–Ni–Co PM piece and two Nd–Fe–B PM pieces) which form a PM pole, and how to determine the dimensions of the outer-rotor. By using the TS-FEM, the machine performances are simulated which well agree with the design principles. Moreover, the experimental results well verify the simulated results under the same working condition, hence confirming the validity of the proposed design principles.

Furthermore, the proposed design principles can readily be applied to other kinds of doubly salient machines with electromagnets or PMs installed in the stator.

Acknowledgment

This work was supported and funded by a research grant (Project HKU 710710E) of the Research Grants Council in Hong Kong Special Administrative Region, China.

References

[1] V. Ostovic, "Memory motors," *IEEE Ind. Appl. Mag.*, vol. 9, no. 1, pp. 52–61, Jan. 2003.
[2] K. Sakai, K. Yuki, Y. Hashiba, N. Takahashi, and K. Yasui, "Principle of the variable-magnetic-force memory motor," in *Proc. Int. Conf. Electr. Mach. Syst.*, 2009, pp. 1–6.
[3] C. Yu and K. T. Chau, "Dual-mode operation of dc-excited memory motors under flux regulation," *IEEE Trans. Ind. Appl.*, vol. 47, no. 5, pp. 2031–2041, Sep./Oct. 2011.
[4] C. Yu and K. T. Chau, "Design, analysis, and control of dc-excited memory motors," *IEEE Trans. Energy Convers.*, vol. 26, no. 2, pp. 479–489, Jun. 2011.
[5] C. Liu, K. T. Chau, and J. Z. Jiang, "A permanent-magnet hybrid brushless integrated-starter-generator for hybrid electric vehicles," *IEEE Trans. Ind. Electron.*, vol. 57, no. 12, pp. 4055–4064, Dec. 2010.
[6] C. Liu, K. T. Chau, and W. Li, "Comparison of fault-tolerant operations for permanent-magnet hybrid brushless motor drive," *IEEE Trans. Magn.*, vol. 46, no. 6, pp. 1378–1381, Jun. 2010.
[7] Y. Gong, K. T. Chau, J. Z. Jiang, C. Yu, and W. Li, "Analysis of doubly salient memory motors using Preisach theory," *IEEE Trans. Magn.*, vol. 45, no. 10, pp. 4676–4679, Oct. 2009.